Chinese Chemical Letters 36 (2025) 110838

Contents lists available at ScienceDirect

Chinese Chemical Letters

journal homepage: www.elsevier.com/locate/cclet

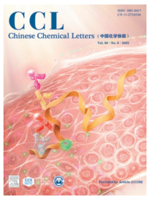

Optimizing $CsPbBr_3$ perovskite solar cell interface and performance through tetraphenylethene derivatives

Sheng Tang[a,1], Mingyue Liao[a,1], Weihai Sun[a], Jihuai Wu[a], Jiamin Lu[b,*], Yiming Xie[a,*]

[a] *Engineering Research Center of Environment-Friendly Function Materials, Ministry of Education, Institute of Materials Physical Chemistry, Huaqiao University, Xiamen 361021, China*
[b] *Clinical Research Institute, the First Affiliated Hospital of Xiamen University, School of Medicine, Xiamen University, Xiamen 361003, China*

ARTICLE INFO

Article history:
Received 12 November 2024
Revised 7 January 2025
Accepted 9 January 2025
Available online 9 January 2025

Keywords:
Perovskite solar cell
$CsPbBr_3$
All-inorganic
Tetra(4-aminophenyl)ethylene
Passivation

ABSTRACT

Recently, $CsPbBr_3$ perovskite solar cells (PSCs) have garnered attention due to cost-effectiveness and reliability. However, hole transport limitations lead to charge recombination and lower power conversion efficiency (PCE). Defects in the $CsPbBr_3$ layer, poor hole transport at the interface with carbon electrodes, and energy level differences hinder performance. Optimizing the perovskite layer using electron-donating organic molecules containing -NH_2 groups enhances efficiency and stability by passivating defects and modulating lattice structure. In this work, tetra(4-aminophenyl)ethylene (TPE) and tetra(4-aminobiphenyl)ethylene (TPE-Ph) were employed to optimize the $CsPbBr_3$/carbon electrode interface. Their strong electron-donating properties and amino groups facilitate hole transfer and defect passivation, boosting PCE to 9.38% and enhancing stability.

Carbon based all-inorganic $CsPbBr_3$ perovskite solar cells (PSCs) have attracted wide attention recently due to their low production cost and great intrinsic reliability [1–3]. However, their hole extraction and transport capabilities are far inferior to perovskite solar cells with a hole transport layer, leading to a significantly higher probability of charge recombination at the interface and thus lower power conversion efficiency (PCE) [4,5].

$CsPbBr_3$ PSCs are predominantly structured with an electron transport layer, the active perovskite layer ($CsPbBr_3$), and a carbon electrode. PSCs prepared with $CsPbBr_3$, which is rich in Br, exhibit a reduction in open-circuit voltage of up to 0.6 V, while $MAPbI_3$ is only 0.3 V, resulting in a significant PCE loss. The efficient and stable performance of $CsPbBr_3$ PSC devices is affected by defects in the perovskite active layer, poor hole transport ability at the interface between the perovskite active layer and the carbon electrode, and the energy level difference between the layers. Therefore, it is important to optimize the perovskite active layer to address these issues and improve the efficiency of $CsPbBr_3$ PSCs. Recently, many electron-donating organic molecules containing -NH_2 groups have been demonstrated to passivate defects by forming coordination bonds with uncoordinated Pb^{2+} and Pb^0 clusters on the surface of the perovskite layer, based on Lewis acid-base chemistry for lattice modulation to enhance efficiency and stability [6–8]. Recent studies have shown that the proton behavior induced by Lewis base-assisted passivation at the interface exerts a significant influence on the lattice structure of hybrid perovskite and the charge transfer kinetics in perovskite solar cells. Utilizing multifunctional organic molecules with -NH_2 groups to enhance the perovskite framework allows for the simultaneous modification of the crystallization process and effective passivation, resulting in a reduction of defect density. Furthermore, the interconnected organic framework contributes to the formation of a moisture-resistant layer on the perovskite surface [9–11]. The optimized mechanism mainly involves coordination reactions with surface dangling Pb^{2+} complex centers. This mechanism modulates the electronic states at the interface, leading to a corresponding alteration in the work function (WF) and valence band position of the perovskite film upon its integration into PSCs. Since the electron-donating ability and stability of surface-optimized molecules depend on specific interactions with the surface, the precise control of molecular structures will determine the overall performance of PSCs.

In this work, amino-functionalized tetraphenylethene derivatives, tetra(4-aminophenyl)ethylene (TPE) and tetra(4-aminobiphenyl)ethylene (TPE-Ph), were used to optimize the interface between $CsPbBr_3$ and the carbon electrode. The results showed that when TPE and TPE-Ph were used to optimize the $CsPbBr_3$/carbon electrode interface, it was found that TPE and TPE-Ph, as strong electron-donating molecules, were beneficial

---

[*] Corresponding authors.
E-mail addresses: lujiamin@zju.edu.cn (J. Lu), ymxie@hqu.edu.cn (Y. Xie).

[1] These authors contributed equally to this work.

https://doi.org/10.1016/j.cclet.2025.110838
1001-8417/

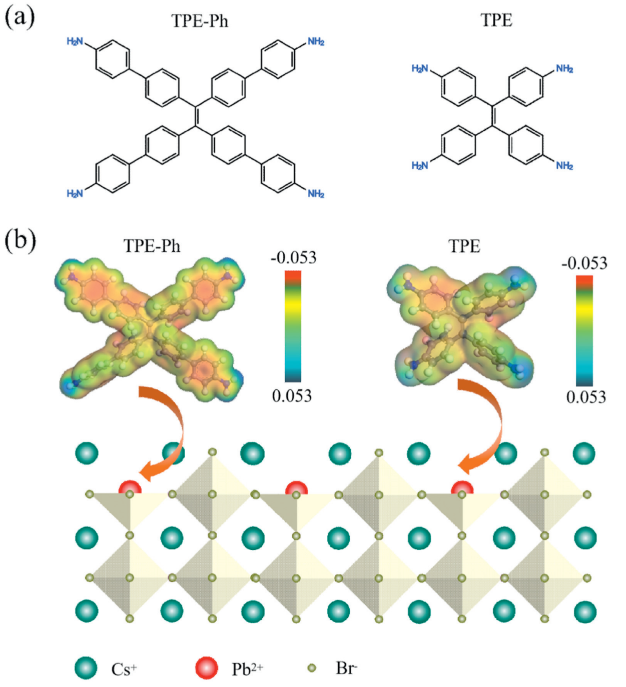

Fig. 1. (a) Structural diagrams of TPE and TPE-Ph. (b) Electrostatic potential distribution images of TPE and TPE-Ph, and schematic illustration of the optimized thin film.

for the hole transfer at the $CsPbBr_3$/carbon electrode interface [12–15]. They have four amino groups at their terminals that can be employed for the passivation of surface defects in the perovskite thin film, greatly increasing the passivation efficiency of the perovskite film defects and improving the stability of the perovskite film. Because the perovskite thin film inevitably exhibits a considerable density of defects and energy barriers that impede charge transfer, by optimizing the perovskite thin film using TPE and TPE-Ph, an internal electric field can be formed to enhance the separation and migration ability of charge carriers, thereby reducing the defects that are inherent to the perovskite film and minimizing the loss of open-circuit voltage [16–19]. These benefits help significantly enhance the power conversion efficiency (PCE) to 9.38% and improve the stability of $CsPbBr_3$ PSCs.

TPEs and TPE-Ph are a class of conjugated macrocycles whose inherent aromaticity makes them an important component of functional supramolecular materials. In this work, TPE and TPE-Ph compounds were used to optimize $CsPbBr_3$ films as shown in Fig. 1a. TPE and TPE-Ph as Lewis bases, along with the conjugated benzene ring, enhance the electron-donating effect of the N atom in the structure. When the molecules were assembled onto the $CsPbBr_3$ surface, they interacted with Pb^{2+} to form a Pb-N bond with Pb^{2+} in the perovskite film due to the electron-donating effect of the amino group on the molecules [20,21]. Compared to TPE, TPE-Ph has more benzene rings, allowing more electrons in the electron-donating benzene ring to be transferred to the amino group, resulting in a stronger electronegativity of the N atom. Therefore, TPE-Ph is more likely to coordinate with the uncoordinated Pb^{2+} on the surface of $CsPbBr_3$ to form Lewis acid-base adducts [22]. The benzene ring of this compound transfers more electrons to the amino group as shown in the electrostatic potential distribution image in Fig. 1b. In other words, the amino group can be thought of as an electron-rich structure and therefore capable of interacting strongly with Pb^{2+}. With its electron-rich structure, it can enhance the hole extraction at the $CsPbBr_3$/carbon electrode interface, thus improving the optoelectronic performance of $CsPbBr_3$ PSCs devices [23,24]. The hole extraction capability and optoelectronic performance will be discussed in detail in the following tests. Thus, this work offers insights into the optimization of perovskite solar cells and serves as a reference for the synthesis of materials with enhanced performance.

The morphology of perovskite films play a crucial role in optoelectronic devices. In order to assess the potential changes in the surface morphology of the perovskite films resulting from optimization with TPE and TPE-Ph, top-view SEM morphological characterization tests were performed. As shown in Fig. 2a, the $CsPbBr_3$ film exhibits large voids before optimization, which can act as a severe charge complexation center in the $CsPbBr_3$ PSCs, increasing the defect density at the interface and leading to a degradation of device performance [25,26]. However, the TPE-optimized perovskite films show a significant reduction of voids and the films become denser after TPE-Ph optimization. The atomic force microscopy (AFM) tests in Figs. 2b and c further demonstrate that the surface roughness of the optimized film is reduced, indicating a smoother surface morphology. This suggests that the optimization process is beneficial in obtaining smooth and high quality perovskite films.

X-ray diffraction (XRD) represents a valuable technique for the investigation of the crystal structure of perovskite films. By performing XRD tests on the perovskite film before and after optimization with TPE and TPE-Ph, the changes in the crystal structure of the perovskite film can be determined. The XRD results of the control and optimized perovskite films are presented in Fig. 3a. Both exhibit diffraction peaks characteristic of the $CsPbBr_3$ phase, including three main peaks near 14.69° (100), 21.08° (110) and 30.04° (200). No positional shifts or additional peaks were observed with the addition of TPE and TPE-Ph, indicating that the tetraphenylethylene derivatives used for optimization had no discernible impact on the crystal structure of the perovskite [27]. However, the diffraction peaks in the TPE and TPE-Ph optimized $CsPbBr_3$ films showed enhanced intensity compared to the unoptimized films. The results indicate that the optimized $CsPbBr_3$ films have higher crystallinity, which is consistent with the observation of SEM tests. This can be attributed to the reduction of grain boundaries in the optimized perovskite film, resulting in lower trap density [28]. These improvements contribute to the photovoltaic performance of $CsPbBr_3$ PSCs.

In order to evaluate the role of TPE-Ph in promoting the performance of $CsPbBr_3$ PSCs, the chemical modification of the surface of the perovskite films before and after optimization was further investigated by XPS spectroscopy. As shown in Fig. 3b, compared with the two characteristic peaks of 138.6 eV (Pb $4f_{7/2}$) and 143.4 eV (Pb $4f_{5/2}$) in the control group, the two characteristic peaks of the perovskite films optimized by TPE-Ph were shifted to 137.5 eV (Pb $4f_{7/2}$) and 142.3 eV (Pb $4f_{5/2}$) toward the position of the low binding energy due to the strong electron-donating effect of TPE-Ph, and the chemical modification of the surface of $CsPbBr_3$ PSCs was further investigated by XPS spectra. The electron-donating effect of TPE-Ph allows Pb^{2+} in the $CsPbBr_3$ film to gain electrons, which enhances the shielding effect and increases the density of the surrounding electron cloud. According to literature reports, the electron donor RNH_2 strongly interacts with uncoordinated Pb^{2+}, which suggests that $-NH_2$ in TPE-Ph has an effective coordination relationship with Pb^{2+}. And, as expected, as shown in the ultraviolet-visible absorption spectra (UV–vis) and the optical bandgap maps obtained from the UV–vis (Figs. 3c and d), the $CsPbBr_3$/TPE-Ph films show significantly increased absorption peak intensities compared to the control perovskite films, which exhibited little change in the bandgap (E_g) of the perovskite films, which is roughly $E_g = 2.36$ eV, indicating that the enhanced crystallinity and improved film quality of $CsPbBr_3$ facilitate greater photon absorption in the perovskite active layer and

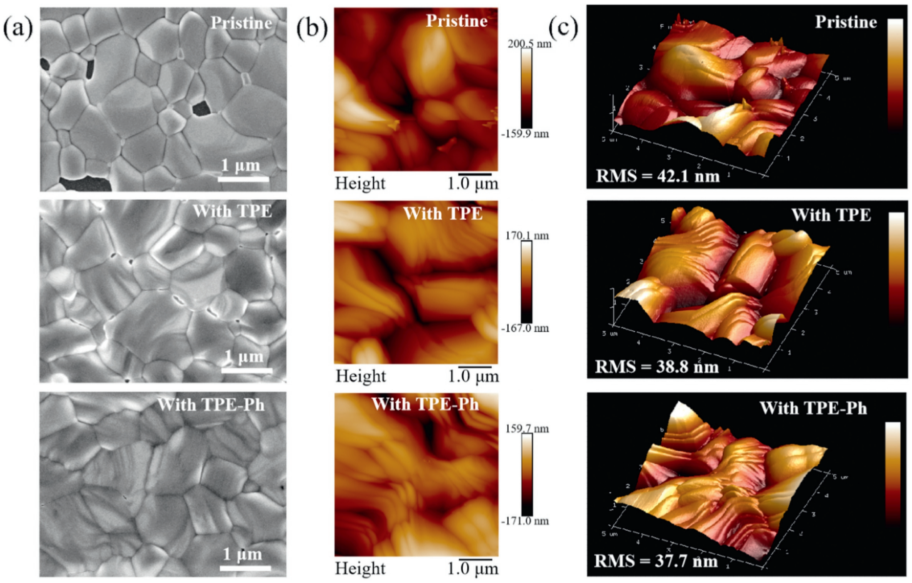

Fig. 2. $CsPbBr_3$ film before and after optimization with TPE and TPE-Ph. (a) SEM images, (b) AFM images, and (c) 3D AFM images.

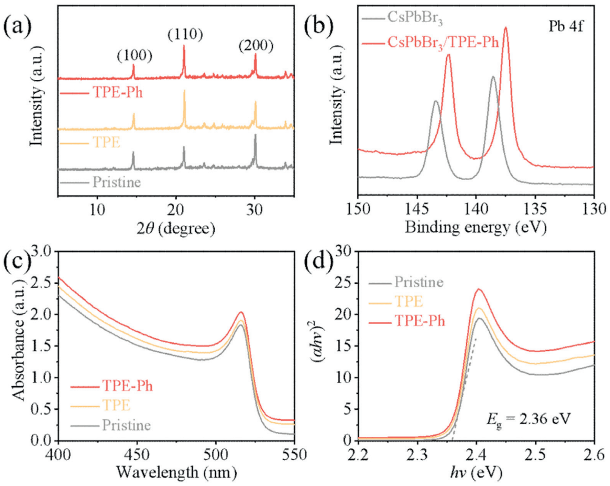

Fig. 3. (a) XRD spectra, (b) XPS spectra, (c) UV–vis spectra, and (d) Tauc plots of $CsPbBr_3$ films before and after addition of the optimized layer.

reduce charge recombination, thereby augmenting the photogenerated current output [29,30].

In order to further examine the surface work function and energy band structure of the films before and after optimization, the energy band positions of the valence band maxima (E_{VBM}) of the perovskite films with $CsPbBr_3$ and $CsPbBr_3$/TPE-Ph structures were determined using ultraviolet photoelectron spectroscopy (UPS), which usually uses ultraviolet light as its excitation source, causing photoelectrons to be emitted from the surfaces of the tested films. Based on the results shown in Figs. S3a and c (Supporting information), the E_{VBM} of $CsPbBr_3$/TPE-Ph is calculated to be −5.56 eV, which is higher than that of the pristine perovskite (−5.63 eV), and will establish a type II cascade structure, which can readily extract photogenerated holes attributed to the insertion of the intermediate energy levels and block the electrons from being trapped at the grain boundaries [31]. Based on $E_g = 2.36$ eV before and after optimization, the conduction band minimum (E_{CBM}) of $CsPbBr_3$/TPE-Ph is −2.427 eV, which is much higher than that of the pristine perovskite, −4.074 eV, and thus effectively blocks the electron transfer. Based on these results, the charge transfer properties and energy band arrangement of the TPE-Ph tailored perovskite films are shown in Fig. S3b (Supporting information).

Steady-state photoluminescence spectroscopy (PL) is a technique used to study charge carrier transport properties in semiconductors and molecular systems. PL measurements recorded the fluorescence intensity of $CsPbBr_3$ films deposited on glass substrates under 385 nm excitation (Fig. 4a). After optimization, the fluorescence intensity of the $CsPbBr_3$ film increased significantly. This indicates a higher number of electrons in the $CsPbBr_3$ films transitioning from the valence band (VB) to the conduction band (CB) after TPE and TPE-Ph optimization. Subsequently, the creation of holes in the VB leads to electron-hole complexation and the production of more photons with higher energies, resulting in stronger photoluminescence. Time-resolved photoluminescence (TRPL) measurements were performed to further evaluate the concentration of electron-hole pairs and their dynamics in $CsPbBr_3$ films before and after optimization. Typically, charge-carrier complexation is characterized by TRPL decay. The normalized TRPL spectra and exponential decay fitting curves are shown in Fig. 4b, and the detailed decay data are listed in Table S1 (Supporting information). The optimized $CsPbBr_3$ film exhibits a longer photoluminescence decay lifetime. This indicates that the charge carriers in the films have longer average lifetimes, resulting in more desirable photoluminescent properties and better film quality. This is consistent with the results and trends observed in the PL tests, in addition to the fact that the TPE-Ph optimized $CsPbBr_3$ films performed better than the TPEs. The decay lifetimes of the carriers in the $CsPbBr_3$ films are closely related to the crystallinity of the perovskite, as the decay process is influenced by the structure and morphology of the perovskite. The crystallinity in turn affects the structure and morphology. This is also consistent with the results and trends observed in the XRD and SEM tests, which further supports the conclusion that the quality of the optimized films is improved and defects are reduced, thus enhancing the photovoltaic performance of the $CsPbBr_3$ PSCs [32].

In order to investigate the defect states of $CsPbBr_3$ PSCs before and after optimization, space charge limiting current (SCLC) analysis was performed to measure the electron trap density. When the bias voltage is low, the current increases linearly with the bias voltage, which is known as ohmic behavior. When the bias voltage exceeds a specific threshold, the trap state is completely filled and the increase in current becomes sharp and nonlinear. The bias

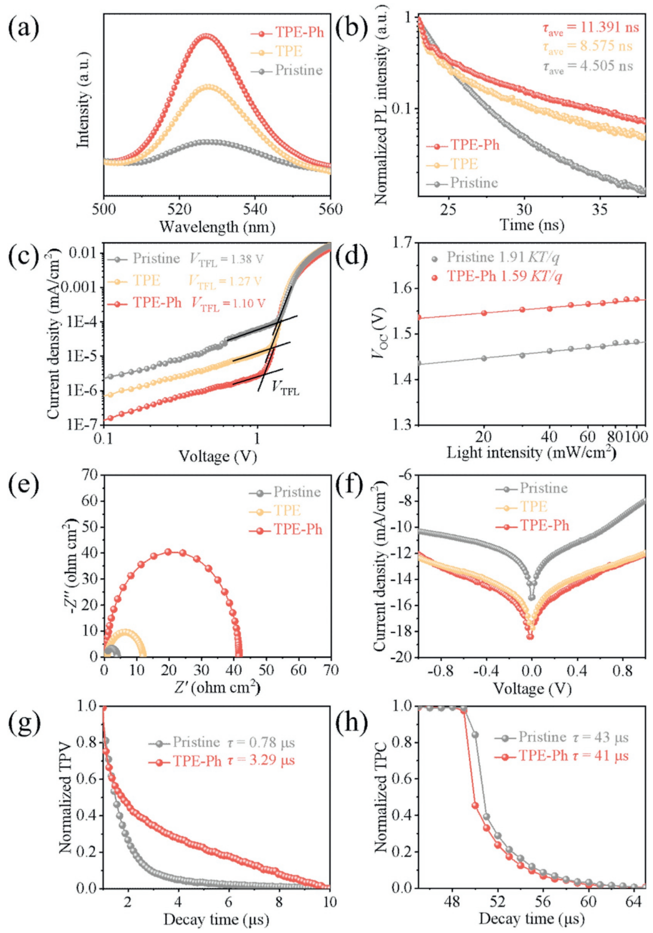

Fig. 4. (a) PL spectra before and after adding the optimization layer, (b) TRPL decay curves, (c) SCLC curves, (d) V_{OC} dependence on light intensity plots, (e) impedance plots in the dark state, (f) *J-V* characteristic curves in the dark state, (g) transient photovoltaic voltage (TPV) decay curves, and (h) transient photocurrent (TPC) decay curves.

voltage at the inflection point is recognized as the trap fill limit voltage (V_{TFL}). From the results in Fig. 4c, it can be seen that the V_{TFL} value of the film without optimization is 1.38 V, while after optimization in TPE and TPE-Ph, the V_{TFL} value decreases to 1.27 V and 1.10 V, respectively. The trap state density can be calculated using equation $n_{trap} = 2\varepsilon\varepsilon_0 V_{TFL}/qL^2$, the trap state density (n_{trap}) can be calculated from the V_{TFL}, where q is the elementary charge, ε_0 is the vacuum permittivity, and ε is the relative dielectric constant, L is the thickness of the $CsPbBr_3$, and the detailed results are listed in Table S2 (Supporting information) [33]. After optimization, the calculated n_{trap} decreased from 1.60×10^{16} cm^{-3} in the control to 1.47×10^{16} cm^{-3} and 1.27×10^{16} cm^{-3}. High defect densities denote charge buildup and poor charge transport at the interface. The significant reduction in defect density after optimization of the perovskite film with electron-donating TPE and TPE-Ph, especially with optimized TPE-Ph containing more benzene rings, and the reduction in the density of defect states after optimization led to an improvement in device performance.

In order to further investigate the charge recombination mechanism of the devices, the *J-V* characteristics at different light intensities were measured in this study. the relationship between V_{OC} and light intensity is shown in Fig. 4d and was calculated by the following equation: $V_{OC}=\frac{nKT\ln(I)}{q}$ + constant, where I is the light intensity, n is the ideality factor, K is Boltzmann's constant, T is the temperature in Kelvin, and q is the charge constant. The TPE-Ph optimized device exhibits a smaller fitting slope of 1.59 KT/q compared to the control device with a slope of 1.91 KT/q. This indicates a reduction in trap-assisted complexation under open-circuit conditions, suggesting improved charge carrier transport in the optimized device [34].

Electrochemical impedance spectroscopy (EIS) measurements were performed to evaluate the charge transfer efficiency and transport resistance, which reflect the charge transfer efficiency at the interface inside the solar cell and reveal the source of performance enhancement. The Nyquist plots and equivalent circuit diagrams of the EIS test results in the dark state are shown in Fig. 4e. The charge recombination resistance (R_{rec}) of the devices optimized with TPE and TPE-Ph is higher than that of the unoptimized devices. Among them, the device optimized with TPE-Ph exhibits the highest R_{rec}, indicating unfavorable charge compounding. This may be attributed to the stronger electron-donating effect of TPE-Ph, which facilitates hole transport at the interface and effectively suppresses interfacial charge compounding, resulting in a larger R_{rec} [35,36]. Fig. 4f shows the *J-V* curves of the devices before and after optimization from 1.0 V to −1.0 V in the dark. It is clear that the optimized devices exhibit lower leakage current densities compared to the unoptimized PSCs, which indicates a reduction in leakage current after optimization.

In addition, the carrier decay was characterized by transient photovoltage (TPV) and transient photocurrent (TPC) measurements. As shown in Fig. 4g, in the TPV test, the $CsPbBr_3$ layer optimized with TPE-Ph exhibits enhanced separation efficiency of photogenerated charges, which makes it easier to transport photogenerated electrons and holes to the electrodes [37]. After TPE pH optimization, the TPV test of the device shows higher transient photovoltage values. As a result, the solar cell optimized with TPE-Ph has a longer charge complex lifetime of 3.29 μs compared to the unoptimized device with a charge complex lifetime of 0.78 μs. This suggests that charge-carrier transport in the target device is faster after TPE-Ph optimization due to the reduction of the defect density and the effective suppression of charge-carrier complexation [38]. In the TPC test of the TPE-Ph optimized device, the transient photocurrent exhibits a smaller value and a shorter charge extraction time. As shown in Fig. 4h, the decay time of the transient photocurrent decreases from 43 μs to 41 μs, which is related to the shorter charge extraction time at the interface in the optimized device.

From the cross-sectional SEM image of the device shown in Fig. 5a, the device exhibits a multilayer structure consisting of a 25 nm SnO_2 layer, a 450 nm monolayer $CsPbBr_3$ light-absorbing layer, and a 10 μm carbon layer. The well-defined monolayer $CsPbBr_3$ light-absorbing layer consists of relatively large $CsPbBr_3$ particles and exhibits an extended longitudinal stacking to form a film morphology. This promotes not only light absorption and carrier generation in the $CsPbBr_3$ PSCs, but also charge transport under illumination, which inhibits charge complexation and enhances effective charge transfer [39,40]. Fig. 5b shows the *J-V* characteristics of $CsPbBr_3$ PSCs before and after optimization with TPE and TPE-Ph, and Table S3 (Supporting information) summarizes the photovoltaic properties. The results show that the optimization resulted in different degrees of parameter improvements for the $CsPbBr_3$ PSCs. In particular, the device with TPE-Ph optimized layer achieved a champion PCE of 9.38%, and the improvement was primarily attributed to the increase in V_{OC} (1.594 V) and *FF* (80.3%), which was significantly higher than that of the unoptimized PSCs (1.550 V for V_{OC}, 0.77% for *FF*, and 7.85% for PCE). The enhancement of V_{OC} and *FF* can be attributed to the TPE-Ph reduction of the trap state density at the interface between the optimized $CsPbBr_3$ perovskite film and the carbon electrode, which reduces the energy loss, facilitates the charge transfer, and reduces the non-radiative recombination at the interface, resulting in improved device performance [41].

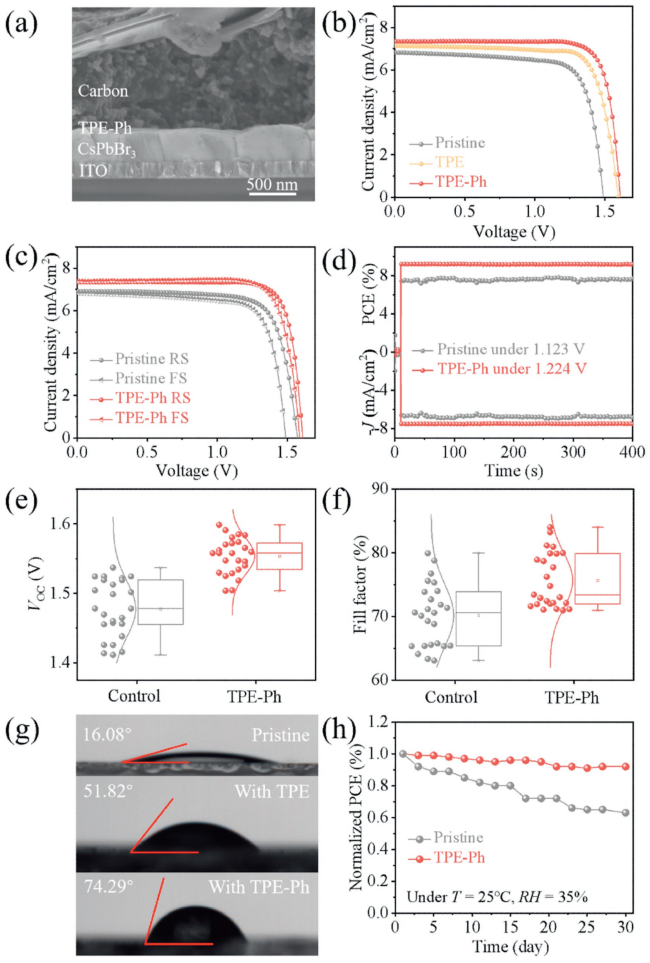

Fig. 5. (a) Cross-sectional SEM image of the complete device after TPE-Ph optimization. (b) *J-V* curves of the devices before and after optimization with TPE and TPE-Ph. (c) *J-V* curves of the devices before and after TPE-Ph optimization in different scan directions. (d) Stable power output curves of the devices before and after TPE-Ph optimization. Statistical distribution of performance parameters before and after optimization: (e) V_{OC} and (f) *FF*. (g) Water contact angle images before and after optimization. (h) PCE degradation trend of the devices before and after TPE-Ph optimization during aging process.

Furthermore, in order to investigate the effect of the TPE-Ph molecules on the device hysteresis, the performance of the device with the introduction of the TPE-Ph-optimized layer was tested under both reverse and forward scans. As shown in Fig. 5c and Table S4 (Supporting information), the obtained results indicate a significant reduction of hysteresis in the optimized PSCs compared to the unoptimized PSCs. The hysteresis factor (HI) of the device was calculated using equation: $HI = \frac{PCE_{reverse} - PCE_{forward}}{PCE_{reverse}}$, and the *HI* value of the optimized device was reduced from 0.07 to 0.009, indicating that the hysteresis was improved with the introduction of TPE-Ph. This enhancement can be ascribed to the reduction of defects and charge recombination in the optimized perovskite film, as well as faster charge transfer, which enhances effective charge transfer and improves device performance, highlighting the positive impact of TPE-Ph on the improved performance of $CsPbBr_3$ PSCs. Steady-state power output tests were performed on the devices before and after the maximum power point optimization to verify the PCE enhancement of the optimized devices [42]. As shown in Fig. 5d, compared with the unoptimized PSCs with a steady-state power output of 7.30% at a maximum power point voltage of 1.123 V and a current density of 6.51 mA/cm^2, the $CsPbBr_3$ PSCs optimized with TPE-Ph exhibited a higher steady-state power of 9.18% at a maximum power point voltage of 1.224 V and a current density of 7.50 mA/cm^2 output, which is consistent with the *J-V* measurements.

In order to explore the effect of TPE-Ph molecular optimization on the reproducibility of the photovoltaic performance of $CsPbBr_3$ PSCs, 25 devices before and after TPE-Ph optimization were selected for photovoltaic performance testing and statistically analyzed (Figs. 5e and f). The experimental results show that the reproducibility of photovoltaic performance is improved to some extent after the optimization of TPE-Ph molecules. In particular, both V_{OC} and *FF* show a significant improvement trend in the experimental data of the 25 optimized devices, indicating a reduction of fluctuations and a convergence of performance values [43]. This indicates that the photovoltaic performance of PSCs can be substantially enhanced *via* optimization of TPE-Ph molecules. After optimization, the average V_{OC} increased by about 0.068 V compared to unoptimized with a small standard deviation. The average value of *FF* also showed significant improvement after optimization with a corresponding decrease in standard deviation. These findings suggest that incorporating TPE-Ph molecularly optimized layers represents an effective strategy for enhancing the photovoltaic performance of $CsPbBr_3$ PSCs, and that this approach demonstrates a high degree of reproducibility.

The hydrophobicity of the perovskite films before and after the addition of the optimized layer was visually assessed by measuring the water contact angle. The results are shown in Fig. 5g, where the water contact angle increased significantly from 16.08° to 51.82° and 74.29° after optimization. This may be attributed to the hydrophobicity of the TPE and TPE-Ph molecules, which is influenced by the covalent bonding between the amino and aromatic groups, allowing water molecules to weakly bind to the surface and form a hydrophobic layer on the perovskite film [44]. Considering its nonlinear ring structure, it also exhibits high hydrophobicity in solution. In order to verify the long-term stability before and after the addition of the optimized layer, the changes in the performance of the unencapsulated $CsPbBr_3$ PSCs before and after the optimization were recorded periodically every two days at 35% humidity to assess the long-term stability after the optimization. The results are shown in Fig. 5h, where the TPE-Ph optimized device exhibited slower PCE reduction compared to the control, retaining 92% of the initial PCE after 30 days, while the control under the same conditions retained only 65% of the initial efficiency after 30 days. One of the reasons for the improved stability of the $CsPbBr_3$ PSCs is the reduction of defects in the optimized device, where TPE-Ph effectively passivated the interfacial defects of $CsPbBr_3$ PSCs and improved charge carrier transport, thus preventing device aging. In addition, the hydrophobic TPE-Ph molecules enhance the hydrophobicity of the $CsPbBr_3$ surface, which improves the stability of $CsPbBr_3$ PSCs [45].

In summary, we have developed a $CsPbBr_3$/carbon interface contact optimization strategy by synthesizing TPE and TPE-Ph as interface optimization layers to enhance the PCE and stability of $CsPbBr_3$ PSCs. Combining SEM, AFM, XRD, PL, and TRPL results, we have found that the introduction of TPE-Ph into the $CsPbBr_3$/carbon interface improves the charge carrier pathways without interfering with the crystal structure. Therefore, we have achieved a device based on $CsPbBr_3$/TPE-Ph/carbon film with a PCE of 9.38%, which is higher than the 7.85% obtained with $CsPbBr_3$/carbon film alone. Further studies indicate that the incorporation of the TPE-Ph optimization layer reduces defects in $CsPbBr_3$ PSCs and enhances the charge carrier transport at the interface, resulting in improved optoelectronic performance and stability of $CsPbBr_3$ PSCs. Thus, this strategy provides a new approach for the development of high-performance $CsPbBr_3$ PSCs.

Declaration of competing interest

The authors declare that they have no known competing financial interests or personal relationships that could have appeared to influence the work reported in this paper.

CRediT authorship contribution statement

Sheng Tang: Investigation, Data curation. **Mingyue Liao:** Writing – original draft, Validation. **Weihai Sun:** Writing – review & editing. **Jihuai Wu:** Writing – review & editing, Resources, Funding acquisition. **Yiming Xie:** Writing – review & editing.

Acknowledgments

This work was supported by the National Natural Science Foundation of China, and the authors sincerely thank the National Natural Science Foundation of China (Nos. 22271106 and 52073286), Science Foundation of State Key Laboratory of Structural Chemistry (No. 20230027). The authors thank the testing service provided by the IACHQU.

Supplementary materials

Supplementary material associated with this article can be found, in the online version, at doi:10.1016/j.cclet.2025.110838.

References

[1] S.S. Mali, J.V. Patil, C.K. Hong, Nano Today 33 (2020) 100880.
[2] W. Xiang, W. Tress, Adv. Mater. 31 (2019) 28.
[3] J. Ding, J. Duan, C. Guo, Q. Tang, J. Mater. Chem. A 6 (2018) 21999.
[4] Y. Sun, W. Chen, Z. Sun, Chin. Chem. Lett. 33 (2022) 1772–1778.
[5] J. Liang, Y.B. Qi, Mater. Today Nano 16 (2021) 100143.
[6] W. Zhang, M. Yuan, L. Han, et al., ACS Appl. Energy Mater. 6 (2023) 7003.
[7] J. Bisquert, Y. Qi, T. Ma, Y. Yan, ACS Energy Lett. 2 (2017) 520.
[8] Y. Yu, P. Gao, Chin. Chem. Lett. 28 (2017) 1144–1152.
[9] C. Liu, L. Zhang, X. Zhou, et al., Adv. Funct. Mater. 29 (2019) 1807604.
[10] X. Qi, J. Wang, F. Tan, et al., ACS Appl. Mater. Interfaces 13 (2021) 55349.
[11] H. Wang, J. Du, X. Li, et al., Chem. Eng. J. 450 (2022) 137990.
[12] J.Y. Kim, J.W. Lee, H.S. Jung, H. Shin, N.G. Park, Chem. Rev. 120 (2020) 7867.
[13] X. Yu, F. Wu, X. Sun, et al., Chin. Chem. Lett. 35 (2024) 109821.
[14] J.P. Correa-Baena, M. Saliba, T. Buonassisi, et al., Science 358 (2017) 739.
[15] M. Lira-Cantu, Nature Energy 2 (2017) 17115.
[16] X. Sun, D. Zhao, Z. Li, Chin. Chem. Lett. 29 (2018) 219–231.
[17] X.L. Xu, L.B. Xiao, J. Zhao, et al., Angew. Chem. Int. Ed. 59 (2020) 19974.
[18] C. Li, H. Li, Z. Zhu, et al., J. Power Sources 537 (2022) 231519.
[19] Y.Y. Zhao, J.L. Duan, Y.D. Wang, X.Y. Yang, Q.W. Tang, Nano Energy 67 (2020) 104286.
[20] K. Zou, Q. Li, J. Fan, et al., ACS Mater. Lett. 4 (2022) 1101.
[21] Y. Wu, C. Lu, F. Gao, et al., J. Mater. Chem. C 11 (2023) 4393.
[22] S.Y. Abate, Z. Yang, S. Jha, et al., ACS Appl. Mater. Interfaces 15 (2023) 25495.
[23] J. Zhu, M. Tang, B. He, et al., J. Mater. Chem. A 8 (2020) 20987.
[24] X. Gong, H. Li, R. Zhou, et al., ACS Appl. Mater. Interfaces 113 (2021) 41149.
[25] J. Ti, J. Zhu, B. He, et al., J. Mater. Chem. A 10 (2022) 6649.
[26] S. Lan, W. Zheng, S. Yoon, et al., ACS Appl. Energy Mater. 5 (2022) 14901.
[27] J. Liang, X. Han, J.H. Yang, et al., Adv. Mater. 31 (2019) 1903448.
[28] J.Y. Chun, B.G. Kim, J.Y. Kim, W. Jang, D.H. Wang, Carbon Energy 5 (2023) 350.
[29] L.K. Ono, N.G. Park, K. Zhu, W. Huang, Y. Qi, ACS Energy Lett. 2 (2017) 1749.
[30] G. Zhang, K. Zhang, Q. Yin, et al., J. Am. Chem. Soc 139 (2017) 2387.
[31] P. Lopez-Varo, J.A. Jimenez-Tejada, M. Garcia-Rosell, et al., ACS Energy Lett. 2 (2017) 1450.
[32] Y. Feng, Z. Que, S. Zhai, et al., Sol. RRL 7 (2023) 2300105.
[33] W. Zhao, Z. Yao, F. Yu, D. Yang, S. Liu, Adv. Sci. 5 (2018) 1700131.
[34] C. Yukta, R. D, D. Prochowicz, et al., ACS Appl. Mater. Interfaces 14 (2022) 850.
[35] S.W. Lee, S. Bae, D. Kim, H.S. Lee, Adv. Mater. 32 (2020) 2002202.
[36] J. Wang, L. Chen, Z. Qian, et al., J. Mater. Chem. A 8 (2020) 25336.
[37] Y. Wang, Y. Li, Z. Gao, et al., ACS Appl. Mater. Interfaces 15 (2023) 53558.
[38] Z. Yi, X. Li, B. Xiao, et al., Chem. Eng. J. 469 (2023) 143790.
[39] T. Kim, R. Younts, W. Lee, et al., J. Mater. Chem. A 5 (2017) 22170.
[40] X. Sun, B. He, J. Zhu, et al., Chem. Eng. J. 412 (2021) 128727.
[41] Y. Li, Y. Guo, Z. Chen, et al., Energy Environ. Sci. 15 (2022) 855.
[42] K.C. Tang, P. You, F. Yan, Sol. RRL 2 (2018) 1800075.
[43] A.N. Cho, N.G. Park, ChemSusChem 10 (2017) 3687.
[44] Y. Gao, W. Xu, F. He, et al., Nano Res. 14 (2021) 2294.
[45] X. Liu, X. Tan, Z. Liu, et al., Nano Energy 56 (2019) 184.